


Electrocatalysis Hot Paper

 How to cite: *Angew. Chem. Int. Ed.* **2021**, *60*, 9590–9597

International Edition: doi.org/10.1002/anie.202015679

German Edition: doi.org/10.1002/ange.202015679

A Robust PtNi Nanoframe/N-Doped Graphene Aerogel Electrocatalyst with Both High Activity and Stability

Jing Yang, René Hübner, Jiangwei Zhang, Hao Wan, Yuanyuan Zheng, Honglei Wang, Haoyuan Qi, Lanqi He, Yi Li, Amare Aregahegn Dubale, Yujing Sun, Yuting Liu, Daoling Peng, Yuezhong Meng, Zhikun Zheng, Jan Rossmeisl, and Wei Liu*

Abstract: Insufficient catalytic activity and stability and high cost are the barriers for Pt-based electrocatalysts in wide practical applications. Herein, a hierarchically porous PtNi nanoframe/N-doped graphene aerogel (PtNiNF-NGA) electrocatalyst with outstanding performance toward methanol oxidation reaction (MOR) in acid electrolyte has been developed via facile tert-butanol-assisted structure reconfiguration. The ensemble of high-alloying-degree-modulated electronic structure and correspondingly the optimum MOR reaction pathway, the structure superiorities of hierarchical porosity, thin edges, Pt-rich corners, and the anchoring effect of the NGA, endow the PtNiNF-NGA with both prominent electrocatalytic activity and stability. The mass and specific activity ($1647 \text{ mA mg}_{\text{Pt}}^{-1}$, 3.8 mA cm^{-2}) of the PtNiNF-NGA are 5.8 and 7.8 times higher than those of commercial Pt/C. It exhibits exceptional stability under a 5-hour chronoamperometry test and 2200-cycle cyclic voltammetry scanning.

Introduction

Breakthrough in fuel cell technologies requires electrocatalysts with both high activity and stability, as well as low cost.^[1] Nevertheless, the state-of-the-art platinum (Pt)-based electrocatalysts still cannot meet these requirements, due to the sluggish kinetics, surface CO poisoning, and catalyst lost caused by aggregation and Ostwald ripening during the

electrocatalysis, and correspondingly the large amount of precious Pt required.^[2] To address these issues, great efforts have been made on the composition, size, and morphology control, structure engineering, and optimization of support materials of the electrocatalysts.^[3] To date, agreement has been reached on how to improve activity, with the general strategies being via increasing the number of active sites and improving the intrinsic activity of each site.^[4] Regarding the electrocatalytic stability, the construction of stabilized Pt alloys, such as alloys with Pt-rich surface,^[1a,5] intermetallic phase,^[6] and high alloying degree,^[7] etc., has been proved to be an efficient way. However, these kinds of electrocatalysts often possess a solid morphology, and the inner Pt atoms are essentially wasted,^[8] resulting in a moderate activity. Recently, the combination of high-porosity one-dimensional Pt-rich surface structure and commercial carbon black (C) support has been demonstrated to be an effective strategy for the preparation of electrocatalysts with both high activity and excellent stability.^[2d,9] The as-developed bunched Pt-Ni alloy nanocages/C electrocatalysts exhibited a superior activity and durability toward oxygen reduction reaction, even in fuel cell tests.^[9] Moreover, it is believed that the electrocatalytic stability of the Pt-based electrocatalysts can be further improved by reasonable design of the support materials, such as via the construction of a porous support structure to facilitate mass transfer and accelerate the intermediates

[*] Dr. J. Yang, Y. Y. Zheng, Y. Li, Dr. A. A. Dubale, Dr. Y. J. Sun, Prof. Y. Z. Meng, Prof. W. Liu
 The Key Laboratory of Low-Carbon Chemistry & Energy Conservation of Guangdong Province, Key Laboratory for Polymeric Composite and Functional Materials of Ministry of Education, State Key Laboratory of Optoelectronic Materials and Technologies, School of Materials Science and Engineering, Sun Yat-sen University
 Guangzhou 510275 (P. R. China)
 E-mail: liuw226@mail.sysu.edu.cn
 Dr. H. L. Wang, L. He, Prof. Z. K. Zheng
 Key Laboratory for Polymeric Composite and Functional Materials of Ministry of Education, School of Chemistry, and State Key Laboratory of Optoelectronic Materials and Technologies, Sun Yat-sen University
 Guangzhou 510275 (P. R. China)
 Dr. R. Hübner
 Helmholtz-Zentrum Dresden—Rossendorf, Institute of Ion Beam Physics and Materials Research
 Bautzner Landstrasse 400, 01328 Dresden (Germany)
 Dr. J. W. Zhang
 State Key Laboratory of Catalysis, Dalian Institute of Chemical Physics, Chinese Academy of Sciences (CAS)
 Dalian 116023 (P. R. China)

Dr. H. Wan, Prof. J. Rossmeisl
 Center for High Entropy Alloy Catalysis (CHEAC), Department of Chemistry, University of Copenhagen
 Universitetsparken 5, 2100 Copenhagen (Denmark)
 Dr. H. Y. Qi
 Center for Advancing Electronics Dresden (cfaed) and Faculty of Chemistry and Food Chemistry, Technical University of Dresden
 01069 Dresden (Germany)
 and
 Central Facility of Electron Microscopy, Electron Microscopy Group of Materials Science, Universität Ulm
 89081 Ulm (Germany)
 Y. T. Liu, Dr. D. L. Peng
 School of Chemistry, South China Normal University
 Guangzhou 510006 (China)

 Supporting information and the ORCID identification number(s) for the author(s) of this article can be found under:
 <https://doi.org/10.1002/anie.202015679>

removal,^[10] heteroatom doping of the support materials to anchor Pt-based electrocatalysts,^[11] and increasing the degree of graphitization of the support to improve corrosion resistance.^[4b] Therefore, it is of great promise to simultaneously achieve long-term stability, high activity, and low cost by constructing highly open and stabilized Pt-based alloy electrocatalysts together with the optimization of the support material. However, this remains a challenge and has been rarely reported.

Pt alloy nanoframes (NFs) have attracted enormous attention due to their prominent electrocatalytic performance endowed by their large surface area per volume, highly open porous architecture that consists of corners and edges, and tunable d-band energy level.^[2c,12] However, the most severe shortcoming of NF electrocatalysts is their insufficient stability.^[13] On one hand, the NF that consists of thin interconnected branches often suffers from a poor intrinsic structural stability, due to a remarkably high surface energy of corner atoms and obvious fragility of the ultrathin edges.^[12b,13] On the other hand, leaching of certain components (especially the non-precious metal), and agglomeration or detachment in a harsh electrochemical condition result in an instability problem during catalysis.^[12f] Recently, attention has been paid to solve the instability problem in the field of NF electrocatalysts, and the introduction of structural support and construction of corner-fortified structures have been proposed.^[12d,f,14] However, sophisticated atomic engineering is often needed, and the corrosion of support materials (usually commercial carbon black) is urge to be resolved.^[13,15] Except for the stability enhancement of the NF corners, that of the NF edges is rarely reported. A step-forward of Pt-based NFs to real commercial use requires further great efforts on enhancing both their activity and especially their intrinsic structural stability and thus the long-term electrocatalytic stability.

Herein, we present an efficient strategy (tert-butanol-assisted PtNi alloy NFs/N-doped graphene aerogel formation strategy) to simultaneously realize exceptional electrocatalytic stability and activity of PtNiNFs in acid electrolyte by an ensemble of several features: a high-alloying-degree-modulated electronic state, Pt-rich corners, and thin edge sizes of the PtNiNFs, the anchoring effect of the N-doped graphene aerogel (NGA) to the PtNiNFs, and the highly exposed hierarchical porous structure of the resulting PtNiNF-NGA. On one hand, the record-small thin edge size, the modulated electronic structure with compressive strain and optimized d-band center, and the highly open structure of the highly alloyed PtNiNF contribute to the high electrocatalytic activity and CO anti-poisoning property. Meanwhile, the high alloying degree of the edges and the Pt-rich corners improve the intrinsic structure stability of the PtNiNFs, slow down the Ni leaching during the electrocatalysis process, and protect the vertices of the NF and significantly fortify the NF structure. On the other hand, the interconnected and highly porous NGA, which is a corrosion-resistant support, enhances the entire mass transfer, anchors the NFs, and avoids the agglomeration or detachment of the NFs in a harsh electrocatalytic condition,^[16] further improving electrocatalytic stability and activity. When applied for methanol oxidation

reaction (MOR), the PtNiNF-NGA shows both outstanding electrocatalytic activity and prominent durability in acid environment (0.1 M HClO₄ solution with 1 M CH₃OH). The mass activity of the PtNiNF-NGA toward MOR is as high as 1647 mA mg_{Pt}⁻¹, which is 5.8 times higher than that of commercial Pt/C (285 mA mg_{Pt}⁻¹). Notably, the PtNiNF-NGA exhibits a significantly enhanced stability toward MOR, and the high activity can be well maintained, even when extending the test time to 5 h or after 2200-cycle cyclic voltammetry scanning. This work provides a new perspective for the preparation of high-performance and cost-effective electrocatalysts.

Results and Discussion

As shown in Figure 1, the PtNiNF-NGA has a hierarchical and highly porous 3D structure constructed by interconnected and crumpled graphene nanosheets with the PtNiNFs uniformly deposited on them, and the introduction of PtNiNFs shows no obvious influence on the highly porous 3D structure of the NGA (Supporting Information, Figure S1), while the PtNiNFs without any support tend to aggregate (Figure S2). The PtNiNFs have an octahedral nanoframe morphology, with an edge thickness of ca. 2.5 nm, an edge length of ca. 8.8 nm, and a hole inside structure. The PtNiNFs have a record-small total size with a narrow size distribution (8.8 ± 1.0 nm; Figure S3).^[12a,e,17] Due to the high edge-thickness-to-length ratio and the very small total size, the superposition of the octahedral edges observed from different viewing directions in projection images leads to different appearances of the PtNiNFs on the GA network, as indicated by the tilted HAADF-STEM micrographs (Figure S4). The element dis-

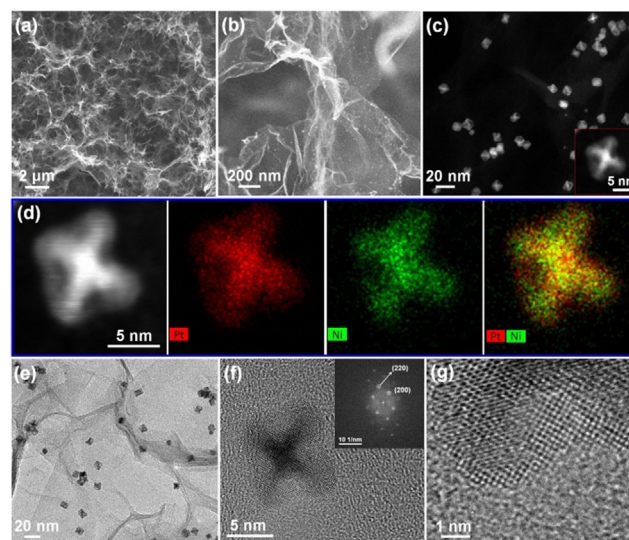
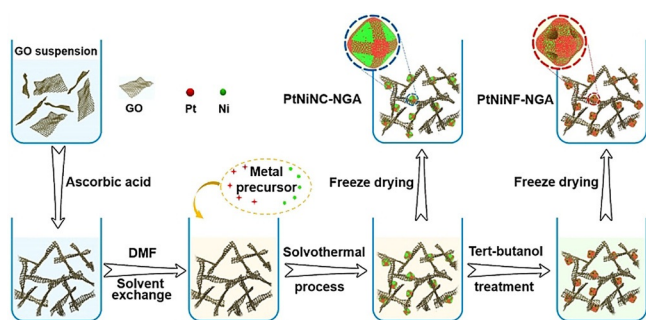


Figure 1. a) and b) SEM images of the PtNiNF-NGA at different magnifications; c) HAADF-STEM micrograph of the PtNiNF-NGA with a PtNiNF enlarged in the lower right inset; d) HAADF-STEM image of the individual PtNiNF on NGA and corresponding EDX-based element maps (Pt: red; Ni: green); e) TEM image; f and g) HRTEM images of an individual PtNiNF. The inset of (f) shows the corresponding FFT pattern.

tribution of Pt and Ni in the PtNiNF was analyzed by EDX-based spectrum imaging analysis in STEM mode (Figures 1 d and S5). The results show the edges of the PtNiNF with uniformly dispersed Pt and Ni and the corners with a Pt-enriched surface. The atom ratio of Pt and Ni obtained from inductively coupled plasma optical emission spectroscopy (ICP-OES) and SEM-EDX (Figure S6) are 52.4:47.6 and 56:44, respectively. A HRTEM image of a PtNiNF and its corresponding FFT are given in Figures 1 f and g. The diffractogram can be described by a [001] zone axis pattern of a face-centered cubic structure with lattice spacings of 0.187 nm and 0.131 nm, which are ascribed to the (200) and (220) planes, respectively. These lattice spacings are a little smaller than those of pure Pt, indicating the presence of compressive strain due to the introduction of Ni into the alloyed structure. ICP-OES characterization shows that the loading of Pt in the PtNiNF-NGA is 8.0 wt %. The short form of PtNiNF-NGA used in the following discussions without specifying the loading amount of Pt means this PtNiNF-NGA (8.0 wt % Pt).

The preparation process of the PtNiNF-NGA is illustrated in Scheme 1, and the evolution of the PtNiNF-NGA was monitored by various techniques. The RGO hydrogel was prepared by using ascorbic acid to chemically reduce the GO without any disturbing. Then, the solvent exchange process was introduced to get the RGO gel filled with DMF. After the solvothermal treatment of the precursor-containing DMF solution in the presence of the RGO gel, nitrogen was doped onto the graphene network, and solid octahedral PtNiNCs were in situ deposited on the N-doped graphene network, as seen from the TEM, HAADF-STEM, and tilted HAADF-STEM images (Figures S7 and S8). Then, the obtained composite gel was washed thoroughly by water and ethanol for several times. The PtNiNCs within the composite gel kept their solid morphology and showed little change during the washing process (Figure S9). From EDX-based spectrum imaging analysis of an individual PtNiNC, it can be seen that the Pt and Ni elements are uniformly distributed along the edges of the octahedron, and the corners are Pt-rich, while the facets and interior of the octahedron are Ni-rich (Figures S10 and S11). After further thoroughly washed by tert-butanol, the composite gel was kept in tert-butanol at 70 °C for 24 h, and the PtNiNF-NGA was finally obtained followed by washing and freeze-drying. Edges and corners with similar elemental distribution to that for the PtNiNC-NGA are



Scheme 1. Illustration of the preparation process of the PtNiNF-NGA.

observed in the PtNiNF-NGA except for the vanished Ni-rich facets (Figures S4 and S5). The ICP-OES measurements show that the atom ratio of Pt and Ni in the PtNiNC-NGA is 44.4:55.6, while that in the PtNiNF-NGA increases to 52.4:47.6. The above results demonstrate the leaching of Ni from the PtNiNC-NGA in tert-butanol. This was further confirmed by UV/Vis monitoring of the tert-butanol supernatant collected after thermal treatment of the PtNiNC-NGA, where oxidized Ni can be detected (Figure S12).^[18] The loading of PtNiNFs on the PtNiNF-NGAs can be adjusted by controlling the concentration of the metal precursors in the mixed solution, where the RGO was immersed into. Besides the PtNiNF-NGA discussed above with 8.0 wt % Pt, PtNiNF-NGAs with 5.2 wt % and 19.4 wt % Pt loadings can be also easily obtained (Figure S13). Further systematic investigations indicate that the initial ratio between the Ni precursor and Pt precursor has great influence on the final PtNi structure. The PtNiNF-NGA was prepared using a Ni/Pt precursor ratio of 1.0:1.3. When the Ni/Pt precursor ratio was decreased to 1.0:4.0, a Pt₂Ni₁-NGA with solid PtNi nanocrystals was obtained. When the Ni/Pt precursor ratio was increased to 4.0:1.0, a Pt₁Ni_{2.6}-NGA with highly open dendrite-like PtNi nanoframes was prepared (Figure S14).

The specific surface areas and porosities of the NGA, PtNiNC-NGA, and PtNiNF-NGA were determined from N₂ physisorption isotherms. The pore size distributions of the NGA and PtNiNC-NGA, analyzed by density functional theory (DFT), are nearly the same, indicating that there are no pore contributions from the solid PtNiNCs (Figures 2 a and S15). Meanwhile, the specific surface area estimated from a Brunauer-Emmett-Teller (BET) plot decreases from ca. 336.1 m² g⁻¹ for the NGA to ca. 300.8 m² g⁻¹ for the PtNiNC-NGA after the introduction of the PtNiNCs (Table S1). As for the PtNiNF-NGA, it shows an increased number of mesopores (ca. 3.8 nm) and much larger BET surface area (ca. 352.0 m² g⁻¹) (Figure 2 a), which further proves the holey structure of the PtNiNFs and is consistent with the HADDF-

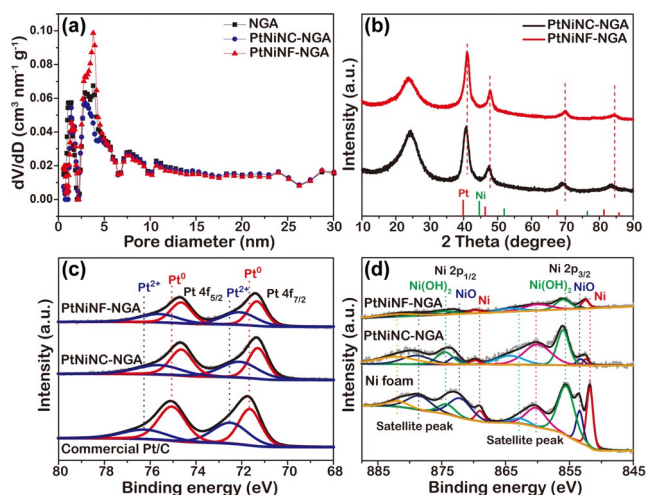


Figure 2. a) Pore size distribution of GA, PtNiNC-NGA, and PtNiNF-NGA; b) XRD patterns of PtNiNC-NGA and PtNiNF-NGA; c) Pt 4f XPS spectra of commercial Pt/C, PtNiNC-NGA, and PtNiNF-NGA; d) Ni 2p XPS spectra of Ni foam, PtNiNC-NGA, and PtNiNF-NGA.

STEM and ICP-OES results. In addition, the content of NiO and Ni(OH)₂ on the surface of the PtNiNF-NGA analyzed by XPS (Figure 2d) are significantly lower than those on the PtNiNC-NGA, demonstrating the diminished NiO and Ni(OH)₂ surface in the Ni leaching process. Based on the above experimental results, and the fact that Ni is easy to be oxidized by dissolved O₂ under ambient condition, as confirmed by the XPS results and literatures,^[12a] and tert-butanol can form soluble complexes with Ni²⁺,^[19] we propose that in the tert-butanol-assisted structure reconfiguration strategy, the synergy of the oxidation effect from the dissolved O₂ to Ni and the complexation effect from the tert-butanol to oxidized Ni drives the leaching of Ni from the solid PtNiNC-NGA to form the holey PtNiNF-NGA.

As shown from the XRD characterizations in Figure 2b, both PtNiNCs and PtNiNFs exhibit a face-centered cubic (fcc) crystal structure. The four specific peaks corresponding to the (111), (200), (220), and (311) lattice planes ($2\theta > 35^\circ$) are located between those for Pt (PDF#04-0802) and Ni (PDF#04-0850), indicating lattice contraction of Pt and the formation of a PtNi alloy in the PtNiNF-NGA.^[12a,20] This is in accordance with the HRTEM results. When compared with the PtNiNC-NGA, the PtNiNF-NGA shows positively shifted peaks, indicating a higher compressive strain and alloying degree in the PtNiNF-NGA, which may be due to an atom rearrangement during the tert-butanol-assisted Ni leaching process.^[7c] The composition and the valence state of the elements on the surface of the PtNiNF-NGA, the PtNiNC-NGA, and commercial Pt/C were characterized by XPS (Figures 2c and d). As for the PtNiNF-NGA, the peaks of Pt 4f_{5/2} and Pt 4f_{7/2} at 74.5 and 71.2 eV are assigned to metallic Pt (54.4%), and the peaks at 75.9 eV and 72.5 eV correspond to Pt²⁺ (45.6%). Notably, the Pt 4f binding energies of both the PtNiNC-NGA and the PtNiNF-NGA are down-shifted compared to those of commercial Pt/C, which indicates the change in the electron density of states of the d-band, and may weaken the adsorption of reaction intermediates on the electrocatalyst surface and in turn enhance their electrocatalytic properties.^[21] Besides, the ratio of Pt to Ni on the surface of the PtNiNF-NGA (70:30) obtained from XPS analysis is higher than that in PtNiNC-NGA (51:49), further demonstrating the Ni leaching during the structure evolution from PtNiNC-NGA to PtNiNF-NGA. The ratios of Pt to Ni in both the PtNiNC-NGA and PtNiNF-NGA obtained from XPS are higher than those from ICP-OES, which can be ascribed to the Pt-rich corners in the PtNiNC and PtNiNF, as shown from the EDX line scan profiles. (Figures S5 and S11). The Ni 2p XPS spectra of the PtNiNC-NGA and PtNiNF-NGA clearly show an increased binding energy when compared with Ni foam, further proving the electron transfer from Ni to Pt (Figure 2d).

Moreover, as shown in Figures S16 and S17, and Table S2, there exist nitrogen sites (ca. 1.0 at% for N) and residual oxygen-containing groups (ca. 8.0 at% for O) on the NGA, which can help binding the PtNiNFs well to prevent the aggregation of them on the graphene network and endow an enhanced catalytic performance during the electrochemical process.^[22] The d-band center shifts of the PtNiNC-NGA and the PtNiNF-NGA vs. Pt in commercial Pt/C were further

calculated from the valence band measured by XPS. The d-band center is closely correlated to surface adsorption of intermediates. As seen in Figure S18, the d-band center of the PtNiNF-NGA is down-shifted, which is attributed to the electron transfer from Ni to Pt, as indicated by the XPS results, and can weaken the CO bonding on the Pt surface by donating more electrons to the Pt–CO antibonding orbital, thereby increasing the catalytic performance.^[23] As for the PtNiNC-NGA, the d-band center is further down-shifted, which can be ascribed to the Ni-rich surface in the facets and interior of the PtNiNCs (Figures S10 and S11).

Furthermore, the X-ray absorption fine structure (XAFS) analyses at the Ni K-edge and the Pt L3-edge for the PtNiNC-NGA and PtNiNF-NGA, and the corresponding Ni foil, NiO powder, Pt foil, and PtO₂ powder references were conducted to examine the valence state and coordination environment of the Ni and Pt atoms. The oxidation state of the metal in a statistical nature can be analyzed from the XANES region based on the edge position and white line intensity.^[24] The results demonstrate that the platinum in both PtNiNC-NGA and PtNiNF-NGA bimetallic alloys is statistically metallic platinum, while the nickel is obviously in oxidation state (Figures 3a and b). The oxidation state of Ni can be ascribed to the synergy effect of electron transfer from Ni to Pt and surface oxidation of Ni. EXAFS was utilized to investigate the local atomic structure and to acquire structural parameters, such as the coordination numbers (CNs), bond lengths, and alloying degree in a bimetallic nanoparticle. As shown from the radial distance space spectra in Figures 3c and S19, the approaching scattering path of Pt–Ni (Ni–Pt) bonds signal in the Pt L3-edge and Ni K-edge in both PtNiNC-NGA and PtNiNF-NGA indicate their bimetallic alloying structure, and the PtNiNF-NGA exhibits more merged scattering path of Pt–Pt (Ni–Ni) and Pt–Ni (Ni–Pt) bonds, indicating a higher alloying degree. Moreover, the wavelet transformation of $\chi(k)$ was conducted to directly demonstrate the alloying degrees in the PtNiNC-NGA and PtNiNF-NGA as compared with the corresponding Ni and Pt foil references (Figures 3d–g). For the Pt L3-edge wavelet transform of the $\chi(k)$ spectra of PtNiNC-NGA and PtNiNF-NGA (Figures 3d and e), only

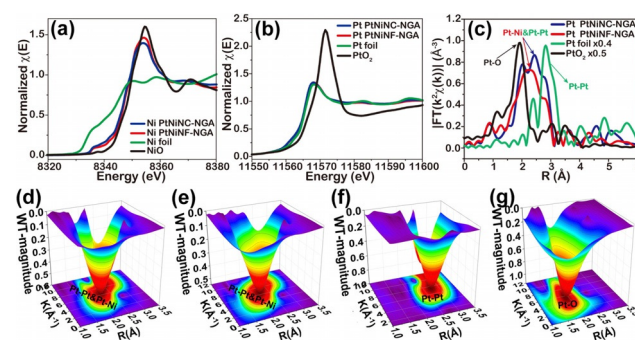


Figure 3. Normalized X-ray absorption near-edge structure (XANES) $\chi(E)$ spectra of PtNiNC-NGA and PtNiNF-NGA: a) Ni K-edge with the Ni foil and NiO as references; b) Pt L3-edge with the Pt foil and PtO₂ as references; c) radial distance $\chi(R)$ space spectra of PtNiNC-NGA and PtNiNF-NGA; 3D contour wavelet transform extended X-ray absorption fine structure (WTEXAFS) map with 2D projection of PtNiNC-NGA (d), PtNiNF-NGA (e), Pt foil (f), and PtO₂ (g).

one merged scattering path signal of Pt–Pt and Pt–Ni bonds located at $[\chi(k), \chi(R)]$ of [6.71, 2.38] and [6.50, 2.28] is observed, respectively. Compared with that of the Pt–Pt bond in the Pt foil ([7.4, 2.82]) (Figure 3 f), both the $\chi(k)$ and $\chi(R)$ of PtNiNC-NGA and PtNiNF-NGA move toward lower values, which can be attributed to the formation of heterogeneous metallic bond (Pt–Ni), and the PtNiNF-NGA shows the lowest values, implying a larger number of Pt–Ni bonds and thus a high alloying degree, as well as large compressive strain. No detectable characteristic scattering path signal of the Pt–O bond at [5.6, 1.94] was observed in both PtNiNC-NGA and PtNiNF-NGA, again clearly indicating the statistically metallic platinum state in them (Figure 3 g).

Quantitative $\chi(R)$ space spectra fitting was performed to investigate the local atomic structure and obtain the CNs of Ni or Pt in the PtNiNC-NGA and PtNiNF-NGA bimetallic alloys (Figure S20 and Table S3). Both the first and the second coordination shell were taken into consideration in Ni K-edge and Pt L3-edge $\chi(R)$ space spectra fitting for the PtNiNC-NGA and PtNiNF-NGA. The combination of $\chi(R)$ and $\chi(k)$ space spectra fitting is the intuitive way to distinguish such merged scattering path signal contributions from each other.^[25] In the Pt L3-edge $\chi(R)$ space spectra, the PtNiNC-NGA displays Pt–Pt bonding with a CN approaching 7.0 and Pt–Ni bonding with a CN approaching 2.5, while the PtNiNF-NGA displays Pt–Pt bonding with a decreased CN approaching 5.0 and Pt–Ni bonding with an increased CN approaching 5.0. The good fitting results of $\chi(R)$ and $\chi(k)$ space spectra with reasonable R-factor and the obtained fitting parameters indicate quantitatively that the PtNiNC-NGA possesses more phase separation and preserves more characteristic homogeneous metallic bonding with higher corresponding Ni–Ni and Pt–Pt CNs (Table S3), while the PtNiNF-NGA exhibits more completely fused state with a higher CN of heterogeneous metallic Pt–Ni (Ni–Pt) bonding. Furthermore, the alloying degree (J) can be calculated quantitatively as in Equation (1):^[26]

$$J_A = P_{\text{observed}}/P_{\text{random}} 100\% \quad (1)$$

where J_A stands for the alloying degree of atom A, P_{observed} is the parameter which can be calculated from the CN of A–B bonding and the total CN of atom A ($P_{\text{observed}} = N_{A-B}/\sum N_{A-i}$), and P_{random} is the parameter of atom-A-based perfect bimetallic alloy under the ideal condition, which can be calculated from the atom number (n) [Eq. (2)].

$$P_{\text{random}} = n_B/(n_A + n_B) 100\% \quad (2)$$

The PtNiNC-NGA shows a lower J_{Pt} (48%) and J_{Ni} (52%), which are both much lower than 100%, implying the inferior distribution of both Ni and Pt atoms in PtNiNCs. In contrast, the PtNiNF-NGA shows significantly increased J_{Pt} and J_{Ni} , which are 104% and 106%, respectively, indicating the improved atomic distribution of both Pt and Ni atoms, and more heteroatomic interactions than homoatomic interactions in the entire PtNiNF-NGA.^[26] This result is highly consistent with the XRD results.

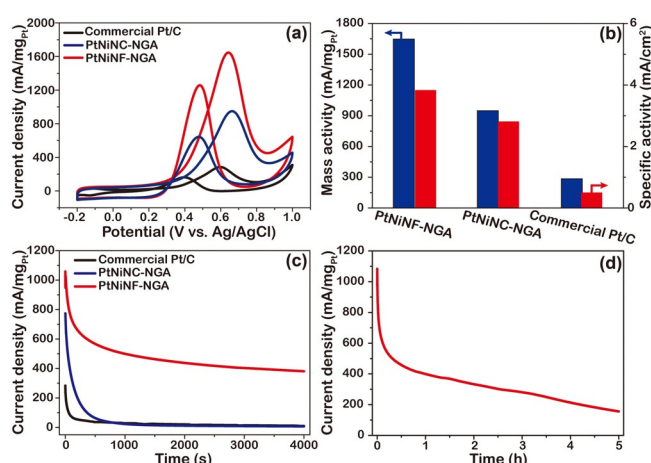


Figure 4. a) CV curves of the commercial Pt/C, PtNiNC-NGA, and PtNiNF-NGA in 0.1 M HClO₄ and 1.0 M methanol solution. Scan rate: 50 mVs⁻¹. b) Mass activities and specific activities of these electrocatalysts. c) Chronoamperometric curves of the commercial Pt/C, PtNiNC-NGA, and PtNiNF-NGA at 0.56 V (vs. Ag/AgCl) for 4000 s. d) Long-term chronoamperometric curve of PtNiNF-NGA at 0.56 V (vs. Ag/AgCl) for 5 h.

The electrocatalytic performances of the PtNiNF-NGA, the PtNiNC-NGA, and commercial Pt/C toward MOR were comparatively measured in N₂-saturated 0.1 M HClO₄ containing 1 M methanol (Figure 4). The mass activity of the PtNiNF-NGA toward MOR is as high as 1647 mA mg_{Pt}⁻¹, which is 1.7 and 5.8 times higher than that of PtNiNC-NGA (949 mA mg_{Pt}⁻¹) and commercial Pt/C (285 mA mg_{Pt}⁻¹), respectively (Figure 4b and Table S4). However, there is no detectable signal for the NGA toward MOR, indicating that pure NGA is inactive toward MOR and the activity of the PtNiNF-NGA is mainly contributed from the PtNiNFs on the 3D NGA network (Figure S21). The specific activity based on the electrochemically active surface area (ECSA) of the PtNiNF-NGA (3.8 mA cm⁻²) is 1.4 and 7.8 times that of the PtNiNC-NGA (2.8 mA cm⁻²) and commercial Pt/C (0.49 mA cm⁻²), respectively (Figures 4b and S22, and Table S5). To the best of our knowledge, the mass and specific activity of the PtNiNF-NGA are among the highest reported values for the Pt-based electrocatalysts, especially the Pt-nonprecious-metal bimetallic electrocatalysts, toward MOR in acid environment (Table S4).

Then, chronoamperometric measurements of all the electrocatalysts were conducted at 0.56 V (vs. Ag/AgCl) in N₂-saturated 0.1 M HClO₄ containing 1.0 M methanol to evaluate their stability (Figure 4c). During the entire time course, the PtNiNF-NGA exhibits a much higher current density than the PtNiNC-NGA and commercial Pt/C. After 4000 s, the current density of the PtNiNF-NGA still retains as high as 381.2 mA mg_{Pt}⁻¹, which is 53 and 37 times higher than that of the PtNiNC-NGA (7.2 mA mg_{Pt}⁻¹) and commercial Pt/C (10.3 mA mg_{Pt}⁻¹), respectively. When the stability test was further extended to 5 h, the PtNiNF-NGA still shows a considerable current density, which is as high as 155.8 mA mg_{Pt}⁻¹ (Figure 4d), the PtNiNFs remain well dispersed on the NGA network, and most of the PtNiNFs maintain their morphology well (Figure S23). Furthermore, the activity of the PtNiNF-

NGA retained as high as 86 % after 2200 CV cycles, while that of commercial Pt/C was only 38 % under the same conditions (Figure S24). This long-term stability of the PtNiNF-NGA is superior to Pt-based electrocatalysts reported recently under acidic conditions (Table S4).

To dig out the reason for the greatly enhanced durability of the PtNiNF-NGA as compared to that of the PtNiNC-NGA and the Pt/C, we further monitored their morphology and composition change after the durability test. It was found that the PtNiNFs in the PtNiNF-NGA maintained their morphology and dispersion well during the 4000-s stability test (Figure S25). Notably, even after the 5 h's durability test (Figure S23), the atom ratio of Pt to Ni for the PtNiNF-NGA was retained at 69:31, and the morphology and dispersion were still maintained well. Moreover, the PtNiNF-NGA kept its crystalline structure well and showed negligible change in size during the long-term stability test (Figure S26). In contrast, for the PtNiNC-NGA, the morphology and size changed, and more serious Ni leaching happened even during the 4000-s stability test (Pt:Ni = 76:24); however, the dispersion of the PtNiNCs on the NGA was maintained. In the case of the commercial Pt/C, there was an obvious aggregation and ripening of Pt nanoparticles (Figure S27), thus demonstrating the important role of the NGA in anchoring the PtNi catalyst to avoid particle mobility and aggregation. XPS spectra were also used to monitor the evolution of the element composition and electronic state of the PtNiNF-NGA during the long-term stability test. The results indicate that the surface leaching of Ni happened during this 5-hour stability test, while the modulated electronic state was well maintained (Figure S28). What is more important, in combination with the XAFS analyses, the results show that the higher alloying degree of Pt and Ni in the PtNiNF-NGA can greatly slow down the leaching of Ni from the PtNiNF-NGA, which is most probably the main origin for the higher durability.

The removal of CO from the surface is vital to increase the stability of Pt-based electrocatalysts toward MOR.^[27] Therefore, CO stripping voltammetry was carried out for commercial Pt/C, PtNiNC-NGA, and PtNiNF-NGA (Figure S29). Compared with commercial Pt/C (0.51 V vs. Ag/AgCl), the PtNiNF-NGA and PtNiNC-NGA show surprisingly similar and much better anti-CO poisoning capability, as indicated by the significantly decreased oxidation peak potential toward CO at 0.45 V vs. Ag/AgCl.^[28] Since both the PtNiNCs and PtNiNFs are anchored on the NGA, the contribution of the NGA support anchoring effect to the stability is believed to be similar, too.

Density functional theory (DFT) predictions of possible mechanistic pathways for the MOR were further conducted to understand the high MOR performance of the PtNiNF-NGA and the difference between the PtNiNC-NGA and the PtNiNF-NGA (Figures 5, S30 and S31). The relative free energies of the most stable surface intermediates on Pt₇Ni₂ (111) and PtNi (111) (following the XPS results for the PtNiNF-NGA and PtNiNC-NGA, respectively) and Pt (111) were calculated. As for Pt (111), its potential-determining step (PDS) is the oxidation of water to form adsorbed *OH (H₂O → *OH + H⁺ + e⁻), which requires 0.76 V.^[29] As shown

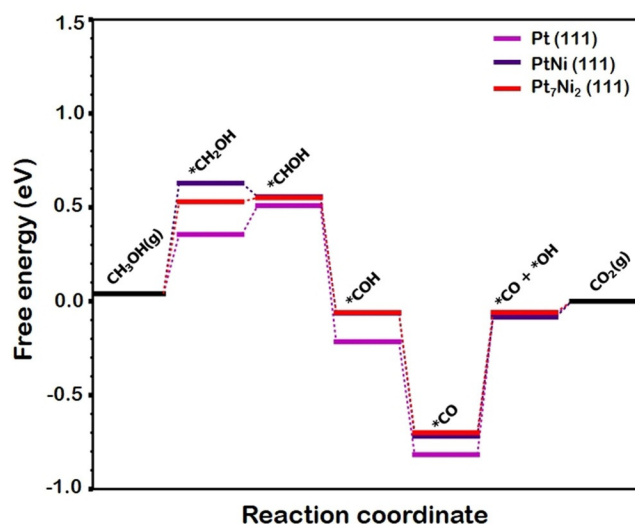


Figure 5. Free energy diagram for the MOR on Pt (111) (purple line), Pt₇Ni₂ (111) (red line), and PtNi (111) (indigo line) with H₂ (g), CO₂ (g), and H₂O (g) as a reference.

in Figure 5 and in the literature,^[30] Pt is poisoned by strongly adsorbed *CO. When it comes to bimetallic PtNi alloys with different compositions, it is obvious that the presence of Ni, on one hand, increases the barrier for forming the adsorbed *CH₂OH intermediate (shown in Figure 5), on the other hand, benefits MOR toward CO₂ by weakening *CO adsorption on the Pt atoms and providing adsorbed *OH as the oxidant at a lower potential on the Ni atoms.^[29] On PtNi (111) with lower alloying degree, the higher content of Ni requires much higher potential for CH₃OH molecule deprotonation to form *CH₂OH, which becomes the PDS (0.64 V). In the case of Pt₇Ni₂ (111) with higher alloying degree, the potential to form *CH₂OH (0.52 eV) is better than for PtNi (111), and notably, Pt₇Ni₂ just requires around 0.61 V to conduct the CO oxidation. Both experiments (similar CO stripping potential in Figure S29) and computational results (in Figure 5) illustrate that the potential for *CO oxidation is similar on Pt₇Ni₂ (111) and PtNi (111). However, Pt₇Ni₂ (111) with higher alloying degree can balance the barriers for *CH₂OH formation and *CO oxidation in a better way. Furthermore, despite a slightly stronger *OH adsorption, a weaker *CO adsorption on Pt₇Ni₂ (111) also chemically promotes a higher driving force toward CO₂ formation, leading to a higher current density shown in Figure 4 a.

The electrocatalytic performances of the unsupported PtNiNFs, the Pt_{2.1}Ni₁-NGA, Pt₁Ni_{2.6}-NGA, PtNiNF-NGA (5.2 wt % Pt), and PtNiNF-NGA (19.4 wt % Pt) toward MOR were further investigated (Figure S21, S32, S33). Compared with these samples, the PtNiNF-NGA (8 wt % Pt) shows greatly enhanced electrocatalytic activity and especially prominent durability. These results further confirm the significant influences of catalyst-support interaction, alloyed state, composition, and the PtNiNF loading amount on the electrocatalytic performances.

Based on the above results, the prominent activity and greatly enhanced durability of the PtNiNF-NGA are proposed to be ascribed to the following reasons: First, the newly

developed tert-butanol-assisted NF formation and structure reconfiguration strategy endows the PtNiNFs supported on the NGA with a high alloying degree and Pt-rich corners. The high alloying degree of Pt and Ni not only leads to an optimized d-band center, compressive strain effect, and correspondingly lowered barrier for forming *CH_2OH and promoted *CO oxidation, which greatly improves the catalyst's intrinsic catalytic activity and durability, but also slows down the Ni-leaching in acidic condition, further significantly enhancing the durability. The Pt-rich corners protect the vertices of the NF and significantly fortify the NF structure. Second, the appropriate ratio of Pt and Ni in the nanoframe and a suitable PtNiNF loading amount on the NGA endow the PtNiNF-NGA with superior electrocatalytic activity (Figure S32 and S33). Third, the hierarchically porous structure of the PtNiNF-NGA consisting of an interconnected macroporous graphene network and highly exposed mesoporous PtNi nanoframes facilitates the mass and electron transfer and the exposure of the active sites. The faster electron transfer in the PtNiNF-NGA is clearly demonstrated by the lowest semi-circle and highest slope of the PtNiNF-NGA in the electrochemical impedance spectroscopy (EIS) results in Figure S34. Fourth, the NGA serves as a corrosion-resistive support for anchoring the PtNiNFs, ensures the uniform dispersion of the PtNiNFs, avoids serious aggregation, prevents Ostwald ripening, and stabilizes the PtNiNFs during the catalytic process, thus increasing the activity and stability (Figures S23, S25, and S27).

Conclusion

We have developed a facile tert-butanol-assisted structure reconfiguration strategy to synthesize hierarchically porous high-alloying-degree PtNi nanoframes supported on N-doped graphene aerogel (PtNiNF-NGA) electrocatalysts with both excellent activity and prominent durability toward methanol oxidation in acidic condition. Systematic structural and compositional characterizations unveil that the surfactant-free solvothermal reaction and the mild in situ tert-butanol leaching during the pretreatment before freeze drying play the key roles in the evolution of the PtNi nanocrystals supported on the N-doped graphene aerogel (PtNiNC-NGA) into the PtNiNF-NGA with high alloying degree. The PtNiNF-NGA shows a hierarchically porous structure consisting of an interconnected porous graphene network and highly exposed mesoporous PtNiNFs with record-small size (ca. 8.8 nm) and thin edges (ca. 2.5 nm). Comprehensive studies including XAFS and DFT calculations indicate that the high alloying degree of Pt and Ni in the PtNiNF-NGA modulates the electronic structure with compressive strain and optimized d-band center, and correspondingly the optimum reaction pathway with balanced barrier for forming *CH_2OH and promoted *CO oxidation, thus leading to prominent electrocatalytic activity and stability toward methanol oxidation in acidic condition. Especially, the high alloying degree of Pt and Ni in the nanoframe also slows down the Ni leaching, and the Pt-rich corners protect the vertices of the NF and significantly fortify the NF structure,

further promoting the remarkable durability enhancement of the PtNiNF-NGA. This work opens up new avenues for designing electrocatalysts with both high activity and durability.

Acknowledgements

Financial supports from the National Natural Science Foundation of China (51801238, 51803241, 51873236, 51803239, and 21701168), the Natural Science Foundation of Guangdong Province (2018A030313458), the National Key Basic Research Program of China (2020YFA0406101), the 100 Top Talents Program-Sun Yat-sen University, Fundamental Research Funds for the Central Universities (19lgpy09) and Dalian high level talent innovation project (2019RQ063) are gratefully acknowledged. Furthermore, the use of the HZDR Ion Beam Center TEM facilities and the funding of TEM Talos by the German Federal Ministry of Education of Research (BMBF; grant No. 03SF0451) in the framework of HEMCP are acknowledged. Besides, BL14W1 beamline of Shanghai Synchrotron Radiation Facility (SSRF) and 1W1B beamline of Beijing Synchrotron Radiation Facility (BSRF) are gratefully acknowledged for providing beamtime. The Center for High Entropy Alloys Catalysis is sponsored by the Danish National Research Foundation centers of excellence, Project DNRF149. The authors thank the XPS group from the surface and structure analysis platform of the Instrumental Analysis & Research Center, Sun Yat-sen University.

Conflict of interest

The authors declare no conflict of interest.

Keywords:

- [1] a) R. Lin, X. Cai, H. Zeng, Z. Yu, *Adv. Mater.* **2018**, *30*, 1705332; b) M. Zhou, C. Li, J. Fang, *Chem. Rev.* **2021**, *121*, 736–795.
- [2] a) S. Y. Ma, H. H. Li, B. C. Hu, X. Cheng, Q. Q. Fu, S. H. Yu, *J. Am. Chem. Soc.* **2017**, *139*, 5890–5895; b) N. Kakati, J. Maiti, S. H. Lee, S. H. Jee, B. Viswanathan, Y. S. Yoon, *Chem. Rev.* **2014**, *114*, 12397–12429; c) J. Li, S. Z. Jilani, H. Lin, X. Liu, K. Wei, Y. Jia, P. Zhang, M. Chi, Y. J. Tong, Z. Xi, S. Sun, *Angew. Chem. Int. Ed.* **2019**, *58*, 11527–11533; *Angew. Chem.* **2019**, *131*, 11651–11657; d) H.-H. Li, Q.-Q. Fu, L. Xu, S.-Y. Ma, Y.-R. Zheng, X.-J. Liu, S.-H. Yu, *Energy Environ. Sci.* **2017**, *10*, 1751–1756; e) L. Xiong, Z. Sun, X. Zhang, L. Zhao, P. Huang, X. Chen, H. Jin, H. Sun, Y. Lian, Z. Deng, M. H. Rümmerli, W. Yin, D. Zhang, S. Wang, Y. Peng, *Nat. Commun.* **2019**, *10*, 3782.
- [3] a) H. L. Liu, F. Nosheen, X. Wang, *Chem. Soc. Rev.* **2015**, *44*, 3056–3078; b) B. E. Hayden, *Acc. Chem. Res.* **2013**, *46*, 1858–1866; c) B. W. Zhang, H. L. Yang, Y. X. Wang, S. X. Dou, H. K. Liu, *Adv. Energy Mater.* **2018**, *8*, 1703597; d) H. Chen, X. Liang, Y. Liu, X. Ai, T. Asefa, X. Zou, *Adv. Mater.* **2020**, *32*, 2002435; e) W. Y. Zhang, Y. Yang, B. L. Huang, F. Lv, K. Wang, N. Li, M. C. Luo, Y. G. Chao, Y. J. Li, Y. J. Sun, Z. K. Xu, Y. N. Qin, W. X. Yang, J. H. Zhou, Y. P. Du, D. Su, S. J. Guo, *Adv. Mater.* **2019**, *31*, 1805833.

- [4] a) Z. W. Seh, J. Kibsgaard, C. F. Dickens, I. Chorkendorff, J. K. Nørskov, T. F. Jaramillo, *Science* **2017**, 355, eaad4998; b) B. Cai, A. Eychmuller, *Adv. Mater.* **2019**, 31, 1804881.
- [5] a) V. Beermann, M. Gocyla, S. Kuhl, E. Padgett, H. Schmies, M. Goerlin, N. Erini, M. Shviro, M. Heggen, R. E. Dunin-Borkowski, D. A. Muller, P. Strasser, *J. Am. Chem. Soc.* **2017**, 139, 16536–16547; b) Y. Ouyang, H. Cao, H. Wu, D. Wu, F. Wang, X. Fan, W. Yuan, M. He, L. Y. Zhang, C. M. Li, *Appl. Catal. B* **2020**, 265, 118606.
- [6] a) W. P. Xiao, W. Lei, M. X. Gong, H. L. Xin, D. L. Wang, *ACS Catal.* **2018**, 8, 3237–3256; b) T. Y. Yoo, J. M. Yoo, A. K. Sinha, M. S. Bootharaju, E. Jung, H. S. Lee, B. H. Lee, J. Kim, W. H. Antink, Y. M. Kim, J. Lee, E. Lee, D. W. Lee, S. P. Cho, S. J. Yoo, Y. E. Sung, T. Hyeon, *J. Am. Chem. Soc.* **2020**, 142, 14190–14200; c) H. Y. Kim, T. Kwon, Y. Ha, M. Jun, H. Baik, H. Y. Jeong, H. Kim, K. Lee, S. H. Joo, *Nano Lett.* **2020**, 20, 7413–7421.
- [7] a) H. Huang, X. Hu, J. Zhang, N. Su, J. Cheng, *Sci. Rep.* **2017**, 7, 45555; b) K. S. Lee, T. Y. Jeon, S. J. Yoo, I. S. Park, Y. H. Cho, S. H. Kang, K. H. Choi, Y. E. Sung, *Appl. Catal. B* **2011**, 102, 334–342; c) J. Zhang, X. Qu, Y. Han, L. Shen, S. Yin, G. Li, Y. Jiang, S. Sun, *Appl. Catal. B* **2020**, 263, 118345.
- [8] J. Park, H. Wang, M. Vara, Y. Xia, *ChemSusChem* **2016**, 9, 2855–2861.
- [9] X. L. Tian, X. Zhao, Y. Q. Su, L. J. Wang, H. M. Wang, D. Dang, B. Chi, H. F. Liu, E. J. M. Hensen, X. W. Lou, B. Y. Xia, *Science* **2019**, 366, 850–856.
- [10] J. Liu, Q. Ma, Z. Huang, G. Liu, H. Zhang, *Adv. Mater.* **2019**, 31, 1800696.
- [11] J. Mao, J. Iocozzia, J. Huang, K. Meng, Y. Lai, Z. Lin, *Energy Environ. Sci.* **2018**, 11, 772–799.
- [12] a) C. Chen, Y. Kang, Z. Huo, Z. Zhu, W. Huang, H. L. Xin, J. D. Snyder, D. Li, J. A. Herron, M. Mavrikakis, M. Chi, K. L. More, Y. Li, N. M. Markovic, G. A. Somorjai, P. Yang, V. R. Stamenkovic, *Science* **2014**, 343, 1339–1343; b) X. Wang, A. Ruditskiy, Y. N. Xia, *Natl. Sci. Rev.* **2016**, 3, 520–533; c) Z. Zhang, Z. Luo, B. Chen, C. Wei, J. Zhao, J. Chen, X. Zhang, Z. Lai, Z. Fan, C. Tan, M. Zhao, Q. Lu, B. Li, Y. Zong, C. Yan, G. Wang, Z. J. Xu, H. Zhang, *Adv. Mater.* **2016**, 28, 8712–8717; d) S. Luo, M. Tang, P. K. Shen, S. Ye, *Adv. Mater.* **2017**, 29, 1601687; e) C. Wang, L. Zhang, H. Yang, J. Pan, J. Liu, C. Dotse, Y. Luan, R. Gao, C. Lin, J. Zhang, J. P. Kilcrease, X. Wen, S. Zou, J. Fang, *Nano Lett.* **2017**, 17, 2204–2210; f) T. Kwon, M. Jun, H. Y. Kim, A. Oh, J. Park, H. Baik, S. H. Joo, K. Lee, *Adv. Funct. Mater.* **2018**, 28, 1706440; g) S. Chen, M. Li, M. Gao, J. Jin, M. A. van Spronsen, M. B. Salmeron, P. Yang, *Nano Lett.* **2020**, 20, 1974–1979.
- [13] T. Kwon, M. Jun, K. Lee, *Adv. Mater.* **2020**, 32, 2001345.
- [14] a) J. Park, M. Kanti Kabiraz, H. Kwon, S. Park, H. Baik, S.-I. Choi, K. Lee, *ACS Nano* **2017**, 11, 10844–10851; b) Y. E. Wu, D. S. Wang, G. Zhou, R. Yu, C. Chen, Y. D. Li, *J. Am. Chem. Soc.* **2014**, 136, 11594–11597; c) S. P. Luo, P. K. Shen, *ACS Nano* **2017**, 11, 11946–11953.
- [15] N. Macauley, D. D. Papadias, J. Fairweather, D. Spornjak, D. Langlois, R. Ahluwalia, K. L. More, R. Mukundan, R. L. Borup, *J. Electrochem. Soc.* **2018**, 165, F3148.
- [16] B. T. Zhang, G. T. Fu, Y. T. Li, L. C. Liang, N. S. Grundish, Y. W. Tang, J. B. Goodenough, Z. M. Cui, *Angew. Chem. Int. Ed.* **2020**, 59, 7857–7863; *Angew. Chem.* **2020**, 132, 7931–7937.
- [17] a) S. P. Chen, Z. Q. Niu, C. L. Xie, M. Y. Gao, M. L. Lai, M. F. Li, P. D. Yang, *ACS Nano* **2018**, 12, 8697–8705; b) H. Jin, Y. Hong, J. Yoon, A. Oh, N. K. Chaudhari, H. Baik, S. H. Joo, K. Lee, *Nano Energy* **2017**, 42, 17–25.
- [18] R. Takahashi, S. Sato, T. Sodesawa, Y. Kamomae, *Phys. Chem. Chem. Phys.* **2000**, 2, 1199–1204.
- [19] M. Munakata, S. Kitagawa, M. Miyazima, *Inorg. Chem.* **1985**, 24, 1638–1643.
- [20] J. B. Wu, J. L. Zhang, Z. M. Peng, S. C. Yang, F. T. Wagner, H. Yang, *J. Am. Chem. Soc.* **2010**, 132, 4984–4985.
- [21] A. B. A. A. Nassr, I. Sinev, M.-M. Pohl, W. Grünert, M. Bron, *ACS Catal.* **2014**, 4, 2449–2462.
- [22] Y. Shao, J. Sui, G. Yin, Y. Gao, *Appl. Catal. B* **2008**, 79, 89–99.
- [23] J. R. Kitchin, J. K. Nørskov, M. A. Barteau, J. G. Chen, *J. Chem. Phys.* **2004**, 120, 10240–10246.
- [24] a) J. Hu, D. Wu, C. Zhu, C. Hao, C. Xin, J. Zhang, J. Guo, N. Li, G. Zhang, Y. Shi, *Nano Energy* **2020**, 72, 104670; b) A. A. Dubale, Y. Zheng, H. Wang, R. Hübner, Y. Li, J. Yang, J. Zhang, N. K. Sethi, L. He, Z. Zheng, W. Liu, *Angew. Chem. Int. Ed.* **2020**, 59, 13891–13899; *Angew. Chem.* **2020**, 132, 13995–14003.
- [25] a) J. Gu, C. S. Hsu, L. Bai, H. M. Chen, X. Hu, *Science* **2019**, 364, 1091–1094; b) Y. Han, Y. Wang, R. Xu, W. Chen, L. Zheng, A. Han, Y. Zhu, J. Zhang, H. Zhang, J. Luo, C. Chen, Q. Peng, D. Wang, Y. Li, *Energy Environ. Sci.* **2018**, 11, 2348–2352; c) Y. Pan, Y. Chen, K. Wu, Z. Chen, S. Liu, X. Cao, W.-C. Cheong, T. Meng, J. Luo, L. Zheng, C. Liu, D. Wang, Q. Peng, J. Li, C. Chen, *Nat. Commun.* **2019**, 10, 4290.
- [26] B.-J. Hwang, L. S. Sarma, J.-M. Chen, C.-H. Chen, S.-C. Shih, G.-R. Wang, D.-G. Liu, J.-F. Lee, M.-T. Tang, *J. Am. Chem. Soc.* **2005**, 127, 11140–11145.
- [27] a) J. T. L. Gamler, H. M. Ashberry, S. E. Skrabalak, K. M. Koczkur, *Adv. Mater.* **2018**, 30, 1801563; b) R. Nagao, R. G. Freitas, C. D. Silva, H. Varela, E. C. Pereira, *ACS Catal.* **2015**, 5, 1045–1052.
- [28] Z. Pan, M. Liu, J. Yang, Y. Qiu, W. Li, Y. Xu, X. Zhang, Y. Zhang, *Adv. Funct. Mater.* **2017**, 27, 1701122.
- [29] J. K. Nørskov, J. Rossmeisl, A. Logadottir, L. Lindqvist, J. R. Kitchin, T. Bligaard, H. Jónsson, *J. Phys. Chem. B* **2004**, 108, 17886–17892.
- [30] a) A. V. Tripković, K. D. Popović, B. N. Grgur, B. Blizanac, P. N. Ross, N. M. Marković, *Electrochim. Acta* **2002**, 47, 3707–3714; b) G. A. Tritsarlis, J. Rossmeisl, *J. Phys. Chem. C* **2012**, 116, 11980–11986.

Manuscript received: November 24, 2020

Revised manuscript received: January 18, 2021

Accepted manuscript online: February 7, 2021

Version of record online: March 17, 2021